DexFormer: Cross-Embodied Dexterous Manipulation via History-Conditioned Transformer

Ke Zhang[1*], Lixin Xu[1*], Chengyi Song[1], Junzhe Xu[1], Xiaoyi Lin[2], Zeyu Jiang[1], Renjing Xu[1†]
[1]The Hong Kong University of Science and Technology (Guangzhou), [2] Wuhan University
[*]Equal contribution, [†]Corresponding author

***Abstract*—Dexterous manipulation remains one of the most challenging problems in robotics, requiring coherent control of high-DoF hands and arms under complex, contact-rich dynamics. A major barrier is embodiment variability: different dexterous hands exhibit distinct kinematics and dynamics, forcing prior methods to train separate policies or rely on shared action spaces with per-embodiment decoder heads. We present DexFormer, an end-to-end, dynamics-aware cross-embodiment policy built on a modified transformer backbone that conditions on historical observations. By using temporal context to infer morphology and dynamics on the fly, DexFormer adapts to diverse hand configurations and produces embodiment-appropriate control actions. Trained over a variety of procedurally generated dexterous-hand assets, DexFormer acquires a generalizable manipulation prior and exhibits strong zero-shot transfer to Leap Hand, Allegro Hand, and Rapid Hand. Our results show that a single policy can generalize across heterogeneous hand embodiments, establishing a scalable foundation for cross-embodiment dexterous manipulation.**

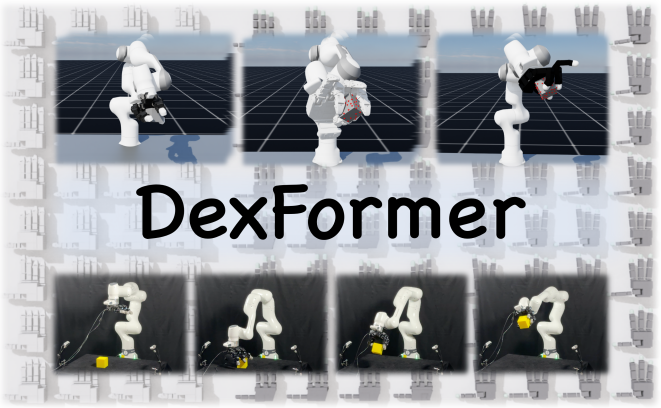

Fig. 1. DexFormer learns a unified history-conditioned policy that transfers dexterous grasping across diverse hand embodiments, enabling zero-shot deployment from large-scale simulation to real-world robots.

I. Introduction

Dexterous manipulation is a key capability for general-purpose robotic manipulation. Multi-fingered robotic hands enable a wide range of functional behaviors, spanning lifting and reorienting everyday objects [13, 18, 29], grasping in clutter [25, 5], non-prehensile manipulation [3, 22], and in-hand reorientation and fine pose adjustment [12, 4, 21, 27]. In practice, however, when transferring to each new hand embodiment typically requires carefully training and tuning a policy from scratch. Different hands induce distinct kinematics, inertias, actuator responses, and contact dynamics, so the same control strategy can lead to drastically different behavior. This embodiment-specific dynamics makes learning and sim-to-real transfer brittle and expensive, often requiring repeated system identification, retuning, or additional real-world data collection for every new platform [12, 4].

The sim-to-real gap is already substantial for a single robot, and becomes even more severe when transferring across different dexterous hand embodiments. Broadly, existing approaches to bridge this gap fall into three paradigms. The first is system identification (SysID), which fits simulator parameters to real hardware through data-driven model identification or active exploration, reducing parameter mismatch between simulation and reality [9, 19]. While effective, SysID is limited by the chosen model parameterization and typically needs to be repeated for each new embodiment. The second paradigm is domain randomization, which trains policies over wide distributions of physical and morphological parameters so that the real world appears as just another sample from training. Massive randomization enabled sim-to-real dexterous in-hand manipulation without real data collection [2], and large-scale RL over procedurally generated robots has produced generalist locomotion policies that control previously unseen robots zero-shot without explicit kinematic knowledge [11]. However, randomization alone does not provide an explicit mechanism to compensate for embodiment-specific dynamics at test time. The third paradigm learns residual or compensatory models for unmodeled dynamics on top of simulation. Methods such as [6] learns unsupervised actuator networks to capture nonlinear hardware effects. Similarly, DexNDM [12] learns a joint-wise neural dynamics model from real interaction data and trains a residual controller on top of a simulation policy, enabling robust dexterous manipulation without precise object state estimation. These residual approaches can significantly narrow the sim-to-real gap, but depend on collecting embodiment-specific real-world data and therefore do not directly address zero-shot cross-embodiment transfer.

In this work, we introduce **DexFormer**, a cross-embodiment dexterous manipulation policy based on a history-conditioned transformer. DexFormer leverages temporal context to perform implicit morphology inference from observation histories, enabling the policy to adapt online to different hand dynamics without explicit morphology identifiers or embodiment-specific heads. We construct a broad morphology distribution via procedural randomization of canonical dexterous hands

and demonstrate that a single morphology-agnostic policy trained on randomized embodiments can *zero-shot* generalize to unseen canonical hands and their variants. DexFormer thus represents a scalable approach to cross-embodiment dexterity and reveals a promising connection between large-scale RL training and history-conditioned models capable of learning latent physical structure.

Our main contributions are summarized as follows:

- We introduce DexFormer, a history-conditioned transformer trained on large scale of hand embodiments, which performs implicit morphology inference for cross-embodiment adaptive control;
- We develop a large-scale morphology-randomization pipeline and a distributed training framework for dexterous hands cross embodiment training;
- We show that a single morphology-agnostic policy can generalize to unseen dexterous embodiments and multiple real dexterous hands without manual retargeting, explicit morphology encodings, or separate policy heads.

II. Related Work

A. Cross-embodiment dexterous manipulation

Cross-embodiment dexterous manipulation has been approached from two main directions. One line of work generates static cross-hand grasp poses followed by open-loop execution, using unified contact representations and optimization or physics solvers to produce feasible grasps across morphologies [23, 24, 28]; however, such open-loop strategies struggle to react to disturbances and real-time contact changes during execution. Others learn embodiment-aware closed-loop controllers, either by explicitly encoding hand kinematic graphs and distilling experts into a single zero-shot policy [15], or by defining an eigen-grasp action space that transfers policies to new hands via retargeting mapping [26]; these approaches depend on explicit kinematic modeling or retargeting mapping and are difficult to extend across fundamentally different canonical hand types. We instead learn a history-conditioned policy in a canonical shared action space that implicitly infers embodiment-specific dynamics from temporal context, enabling closed-loop, zero-shot transfer across heterogeneous hands without explicit morphology encoding or retargeting.

B. Dynamics-aware manipulation

Methods in this direction explicitly model or compensate for mismatches between simulated and real dynamics. Unsupervised Actuator Networks (UAN) [6] learn data-driven corrections to simulator actuator models from real-world trajectories, improving sim-to-real transfer by reducing exploitation of simulator inaccuracies in highly dynamic loco-manipulation. DexNDM [12] instead learns a joint-wise neural dynamics model from autonomously collected real interaction data and uses it to train a residual controller on top of a simulation policy, enabling robust in-hand rotation across diverse objects without precise object state estimation. Complementarily, Zhao et al. [30] narrows the sim-to-real gap by enriching simulation with calibrated actuator and tactile dynamics, combining high-fidelity tactile simulation, current–torque calibration, and randomized motor nonidealities to train force-aware policies that deploy zero-shot on real hardware. These approaches rely on either explicit real-world dynamics learning or highly accurate simulator modeling. Our method avoids additional dynamics models or residual adaptation by training a single policy over a broad, randomized morphology and dynamics distribution and letting temporal context implicitly capture embodiment-specific behavior.

C. Test-time adaptation

Test-time and online adaptation has been extensively studied in legged locomotion and is beginning to appear in manipulation. Rapid Motor Adaptation (RMA) [7] learns a latent embedding online from recent state–action history and conditions a base policy on this latent embedding to rapidly compensate for unmodeled dynamics without additional real-world rollouts or calibration. Variants of this idea have been applied to bipedal robots [8], manipulator arms [10], and dexterous in-hand rotation [16], showing that short temporal histories can support fast system identification and closed-loop correction under changing contacts and loads. In parallel, in-context adaptation with sequence models such as LocoFormer [11] conditions policies directly on history to achieve zero-shot adaptation across terrains and tasks without an explicit identification module. In our setting, we do not explicitly learn a separate adaptation module to suit each environment, but instead learn one history-conditioned policy to a wide distribution of procedurally randomized hand morphologies during training, so that it implicitly infers embodiment-specific dynamics from temporal context and can zero-shot generalize to unseen hand embodiments.

III. Method

A. Problem Formulation

We model dexterous manipulation as a POMDP in which a robotic hand must grasp and stably manipulate objects drawn from a task distribution. Each episode samples an object $o \in \mathcal{O}$ and a hand embodiment $e \in \mathcal{E}$, inducing morphology-dependent transition dynamics.

We aim to learn a morphology-agnostic policy π_θ that receives observations but does not observe the embodiment identity. Let o_t denote the observation of the system at time t, including the hand, arm, and object pointcloud, and a_t denote the action selected by the policy at time t. The reinforcement learning objective is to maximize the discounted reward over the joint distribution of embodiments and objects:

$$\max_{\theta} \ \mathbb{E}_{e\sim p(\mathcal{E}),\, o\sim p(\mathcal{O}),\, \tau\sim\pi_\theta} \left[\sum_{t=0}^{T} \gamma^t R(o_t, a_t) \right], \qquad (1)$$

where R rewards successful grasping behaviors. Since the embodiment is unobserved, the agent must infer morphology-dependent dynamics through temporal interaction and adapt its control accordingly.

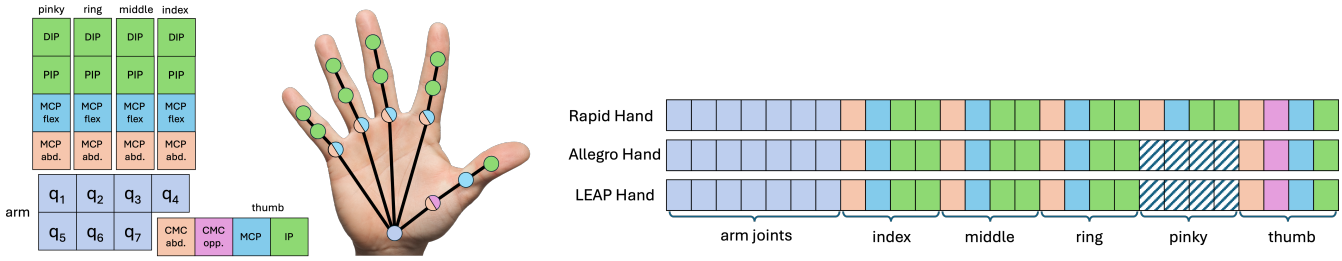

(a) Shared action space and anatomical correspondence.

(b) Shared action space with masks for specific embodiments.

Fig. 2. Shared action space. (a) The canonical action space (left) defines a morphology-invariant embedding in which joints with the same anatomical function share fixed indices in the action space. MCP (blue/orange) governs flexion and abduction, PIP/DIP (green) provide proximal/distal flexion, while the thumb uses a distinct structure where CMC (orange/purple) supports abduction and opposition, MCP (blue) controls basal flexion, and IP (green) provides distal flexion. (b) Canonical embedding flattened into 20-Dim space. Lower-DoF hands such as LEAP and Allegro hands zero-pad unused canonical dimensions, where as higher-DoF embodiments like Rapid Hand fully populate the embedding, enabling shared control across heterogeneous embodiments.

B. Shared Action Space

We consider a family of dexterous robotic hands with different numbers of actuated finger joints. Let $\mathcal{E}$ denote the set of hand embodiments and, for each embodiment $e \in \mathcal{E}$, let d_e be the number of actuated finger joint DoF. To enable a unified control interface across heterogeneous hands, we define a canonical D_F-dimensional finger action space, where joints with the same functional role (e.g., thumb abduction, index flexion) are assigned to the same canonical indices across embodiments.

For embodiment e with d_e actuated finger joints, we denote its native finger command by $\tilde{a}_t^F(e) \in \mathbb{R}^{d_e}$. We embed this command into the canonical action space via a fixed embedding operator

$$P_e : \mathbb{R}^{d_e} \to \mathbb{R}^{D_F},$$

which writes the d_e joint commands into embodiment-specific canonical indices corresponding to their functional roles, such as MCP abduction and flexion ordering, and sets all remaining entries to zero:

$$a_t^F = P_e\big(\tilde{a}_t^F(e)\big) \in \mathbb{R}^{D_F}.$$

Embodiments with fewer finger DoF use zero-padding for unused canonical dimensions, while higher-DoF hands may occupy all or most of the D_F indices, as shown in Fig. 2.

We further apply temporal smoothing to obtain the executed finger action. Let $\hat{a}_t^F \in \mathbb{R}^{D_F}$ denote the raw finger action output by the policy. The smoothed finger command is defined as

$$a_t^F = \lambda\, \hat{a}_t^F + (1-\lambda)\, a_{t-1}^F, \tag{2}$$

where $\lambda \in (0, 1]$ controls the degree of action smoothing.

The overall high-level action at time t is then given by

$$a_t \triangleq \big[a_t^F,\, a_t^A\big] \in \mathbb{R}^{D_F + D_A}, \tag{3}$$

where $a_t^A \in \mathbb{R}^{D_A}$ is the robotic arm delta pose (e.g., $D_A = 7$ for a 7-DoF arm). This shared high-level action is consumed by embodiment-specific low-level controllers, which map a_t to torques or joint targets; zero-padded finger dimensions are simply ignored for lower-DoF hands. In our experiments (Section IV), we instantiate this formulation with a specific choice of D_F and a concrete set of hand embodiments.

C. Embodiment Generation

We construct a family of dexterous hand embodiments by perturbing morphology-related physical parameters of canonical hands. Let $\mathcal{E}_{\text{canon}}$ denote the set of canonical embodiments and, for each $e \in \mathcal{E}_{\text{canon}}$, let $z(e)$ represent its morphology parameters including link lengths, masses, and inertias. We sample randomized embodiments according to

$$z^{(k)}(e) \sim p_{\text{morph}}(z \mid e), \quad k = 1, \ldots, N_e,$$

where p_{morph} is a perturbation distribution defined over morphology parameters. Each sampled morphology $z^{(k)}(e)$ induces a new embodiment $e^{(k)}$, while preserving the original kinematic graph topology and actuation structure.

The union of these embodiments

$$\mathcal{E}_{\text{train}} = \bigcup_{e \in \mathcal{E}_{\text{canon}}} \{e^{(1)}, \ldots, e^{(N_e)}\}$$

forms the morphology-rich training set used for reinforcement learning.

Training on $\mathcal{E}_{\text{train}}$ exposes the policy to a continuum of physical realizations, promoting robustness and improving zero-shot transfer to unseen canonical embodiments at evaluation time.

D. History-Conditioned Transformer

To infer latent morphology parameters that are unobservable from a single state, we condition the policy on a finite history window. Let h_t denote the history available at time t, consisting of past observation-action pairs and the current observation:

$$h_t = \{o_k\}_{k=t-H+1}^{t}$$

We process this history as a sequence of H temporal tokens. For each timestep $k \in [t-H+1, t]$, we construct tokens by using the embeddings of the observation o_k.

This sequence, supplemented with learned positional encodings, is fed into a Transformer encoder. Crucially, we apply a *causal mask* to the self-attention mechanism, ensuring that

the computation for any token k can only attend to preceding tokens $j \leq k$. This prevents information leakage from the future. The Transformer produces a sequence of contextualized latent embeddings. The final embedding, corresponding to the current time t, serves as a compact summary of the history and is passed through an MLP action head to produce the action distribution for a_t, as illustrated in Fig. 3.

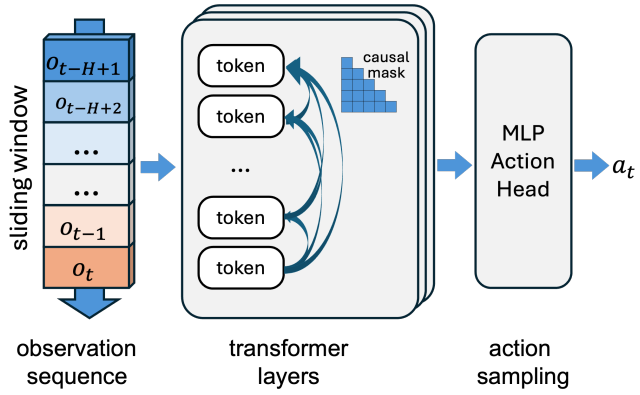

Fig. 3. History-conditioned transformer policy architecture. At each timestep, a fixed-length history of observations with horizon H is provided as input and tokenized into a sequence of H tokens. The token sequence is processed by a stack of three transformer layers with positional encoding and causal self-attention. The representation of the final embedding, which attends to all preceding history, is extracted and passed to an MLP action head to parameterize a stochastic policy. Actions are then sampled from the resulting distribution for execution.

E. Observation Space

The observation space of this policy is defined as

$$o_t \triangleq \left[o_t^{OC}, o_t^{OT}, a_{t-1}, o_t^{JP}, o_t^{JV}, o_t^{FT}, o_t^{FC}, o_t^{V}\right] \in \mathbb{R}^{377}, \tag{4}$$

where the current object quaternion $o_t^{OC} \in \mathbb{R}^4$, the target object pose $o_t^{OT} \in \mathbb{R}^7$, the action $a_{t-1} \in \mathbb{R}^{27}$ at the previous time step, $o_t^{JP} \in \mathbb{R}^{27}$ include the joint positions, $o_t^{JV} \in \mathbb{R}^{27}$ velocities, fingertip and palm states $o_t^{FT} \in \mathbb{R}^{78}$, and contact forces $o_t^{FC} \in \mathbb{R}^{15}$, and object pointcloud $o_t^{V} \in \mathbb{R}^{192}$.

F. Reward Design

The total reward is composed of five terms:

$$r_t = r_t^P + r_t^D + r_t^M + r_t^T + r_t^S, \tag{5}$$

where r_t^P penalizes excessive actions to ensure smooth control, r_t^D encourages the end-effector to approach the object, r_t^M encourages the fingers to grasp the object, r_t^T guides pose tracking under contact, and r_t^S guides pose tracking without contact.

Here, a_i and a_i^{prev} denote current and previous actions, $\mathbf{p}_{\text{ee}}$ and $\mathbf{p}_{\text{obj}}$ are the end-effector and object positions, $\mathbb{I}_c$ indicates valid contact, $\mathbb{I}_m$ encourage exposure to object, $\mathbf{f}_{\text{thumb}}$, $\mathbf{f}_{\text{index}}$, $\mathbf{f}_{\text{middle}}$, and $\mathbf{f}_{\text{ring}}$ are contact force vectors measured at the thumb, index, middle, and ring fingertips respectively, $\tau = 1$ is the force threshold, and $d_q(\cdot)$ measures quaternion distance. λ_1=0.005, λ_2=0.005, λ_3=2, λ_4=0.8, λ_5=2, λ_6=14.0, λ_7=20, σ_{p0}=0.2 and σ_{p1}=0.1 .

TABLE I
REWARD TERMS AND FORMULATIONS.

Term	Equation
r^P	$-\lambda_1 \sum_i a_i^2 - \lambda_2 \sum_i (a_i - a_i^{\text{prev}})^2$
r^D	$\lambda_3 (1 - \tanh\left(\frac{\max \lVert \mathbf{p}_{\text{ee}} - \mathbf{p}_{\text{obj}} \rVert_2}{\sigma}\right))$
$\mathbb{I}_m$	$\mathbb{I}\left[(\lVert \mathbf{f}_{\text{thumb}} \rVert > \tau \vee \lVert \mathbf{f}_{\text{index}} \rVert > \tau \vee \lVert \mathbf{f}_{\text{middle}} \rVert > \tau \vee \lVert \mathbf{f}_{\text{ring}} \rVert > \tau)\right]$
$\mathbb{I}_c$	$\mathbb{I}\left[(\lVert \mathbf{f}_{\text{thumb}} \rVert > \tau) \wedge (\lVert \mathbf{f}_{\text{index}} \rVert > \tau \vee \lVert \mathbf{f}_{\text{middle}} \rVert > \tau \vee \lVert \mathbf{f}_{\text{ring}} \rVert > \tau)\right]$
r^M	$\lambda_4 \mathbb{I}_m + \lambda_5 \mathbb{I}_c$
r^T	$\lambda_6 (1 - \tanh \frac{\lVert \mathbf{p}_{\text{obj}} - \mathbf{p}_{\text{des}} \rVert_2}{\sigma_{p0}}) \mathbb{I}_c$
r^S	$\lambda_7 (1 - \tanh \frac{\lVert \mathbf{p}_{\text{des}} - \mathbf{p}_{\text{obj}} \rVert_2}{\sigma_{p1}})^2$

G. Parallelism for Cross-Embodiment Training

Simulation platforms such as IsaacLab support parallel environments on a single GPU, it expects similar kinematic topology and actuator structure within each GPU, which is not satisfied across different hand embodiments. To accommodate this, we group randomized variants of the same canonical embodiment on a single GPU and assign morphologically distinct canonical embodiments to different GPUs. Rollouts are performed independently on each GPU, and we employ Distributed Data Parallel (DDP) to maintain a single shared policy: during the trajectory collection and forward pass, each GPU operates locally, while during backpropagation gradients are synchronized all-reduce to ensure consistent parameter updates. This configuration parallelizes morphology diversity across GPUs and environment parallelism within GPUs, enabling scalable cross-embodiment training of a single DexFormer policy, as shown in Fig. 4.

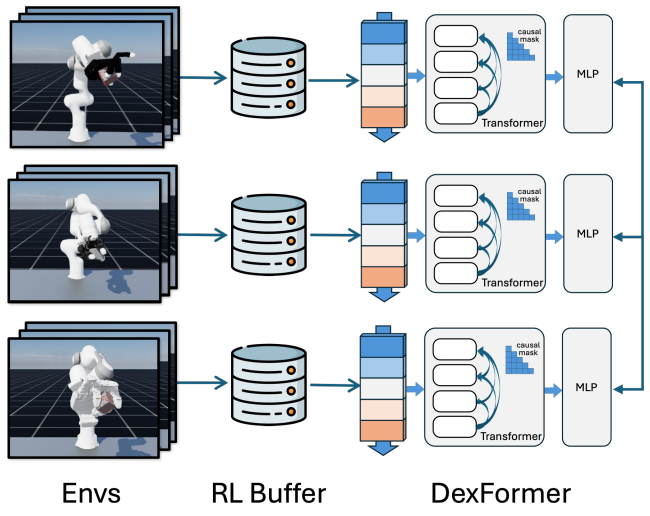

Fig. 4. Gradient aggregation during distributed training. While rollouts and forward passes are computed locally on independent GPUs, the all-reduce primitive aggregates gradients during backpropagation, averaging parameter updates to ensure the DexFormer weights remain identical across all devices.

IV. Experiments

This section presents comprehensive simulation and real-world evaluations of DexFormer's performance on unseen embodiments. Our experiments are designed to systematically answer the following research questions: (1) How does DexFormer's grasp success compare to GRU/LSTM baselines? (2) How well does DexFormer zero-shot generalize across heterogeneous hands? (3) Does historical context improve policy performance? (4) How does embodiment diversity, measured by number of embodiments in training set, affect zero-shot performance? (5) Does performance scale with training parallelism (as measured by number of environment)? (6) How robust is DexFormer to morphological impairments induced by locking individual joints?

A. Implementation Details

We utilize Isaac Lab [14] for both training and evaluation. We use Allegro, LEAP [17], and RAPID [20] hands mounted on Franka Arms as the canonical embodiments:

- Franka-Allegro-Canonical
- Franka-Leap-Canonical
- Franka-Rapid-Canonical

And then we instantiate morphology-randomized variants of the canonical hands:

- Franka-Allegro-Variants
- Franka-Leap-Variants
- Franka-Rapid-Variants

where link lengths and inertial parameters are procedurally perturbed while preserving kinematic and actuation structure. We leverage a ray-casting pipeline built upon Project Instinct [31] to generate point-cloud observations of both dexterous embodiments and manipulated objects.

We train on 300 randomized embodiments in total, corresponding to 100 variants per canonical hand, shown in Fig. 5(a). variants form a morphology-rich training distribution for learning a single cross-embodiment policy. Evaluation is conducted in two settings: (i) zero-shot transfer to the three canonical embodiments, and (ii) generalization to 32 unseen embodiments sampled from the same morphology distribution, shown in Fig. 5(b). For each parallel simulation environment, we randomly sample one object from a predefined set of ten objects, shown as in Fig. 6.

Training is performed on three RTX 5090 GPUs. Variants of the Allegro, LEAP, and RAPID hands are assigned to separate GPUs to satisfy batching constraints in Isaac Lab, while Distributed Data Parallel (DDP) synchronizes gradients across GPUs via all-reduce to maintain a single shared policy. We additionally employ Automatic Domain Randomization (ADR) [1] with a per-environment scheduler that adjusts difficulty levels (0–10) based on task performance.

B. Metrics and Baselines

We evaluate policy performance based on *success rate*, defined as the proportion of trials in which the target object reaches the commanded goal position, i.e., $\|p^{\text{goal}} - p^{\text{target}}\|_2 < 0.05$.

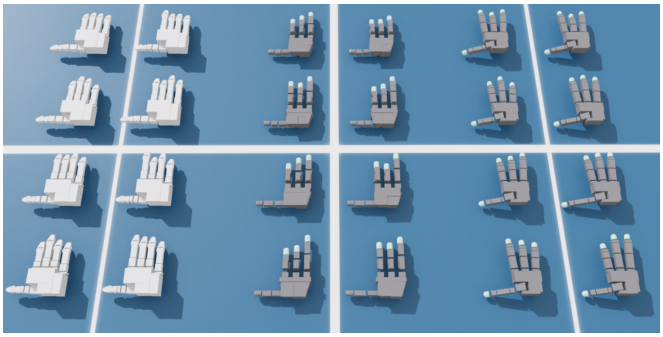

(a) Training embodiment variants (out of 100 for each canonical hand)

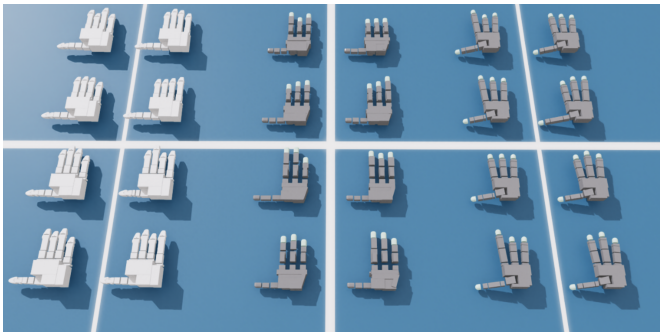

(b) Testing embodiment variants (out of 32 for each canonical hand)

Fig. 5. Diversified embodiment generation. We synthesize 100 variants per canonical LEAP, Allegro, and RAPID hand for training, and 32 variants per canonical hand for testing. Canonical hands are held out during training and evaluated zero-shot.

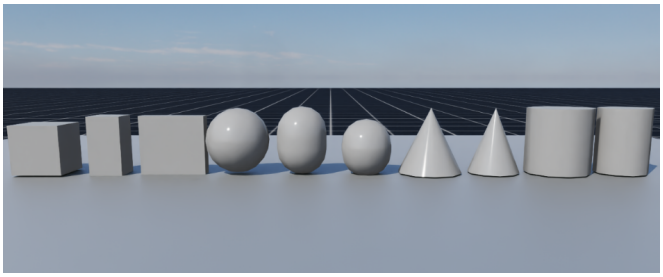

Fig. 6. Objects used during training

We compare DexFormer against two recurrent policy baselines that use explicit hidden states to encode temporal context:

- **LSTM baseline:** a 3-layer LSTM with hidden size 128 is used as the temporal memory module, maintaining cell and hidden states across timesteps to capture longer-range dependencies in the observation history.
- **GRU baseline:** a 3-layer GRU with hidden size 128 replaces the LSTM with a lighter gated recurrent architecture, using a single hidden state to model temporal dependencies.

C. Main Results.

We first evaluate the overall effectiveness of DexFormer under the standard training setting with 5-step history. All

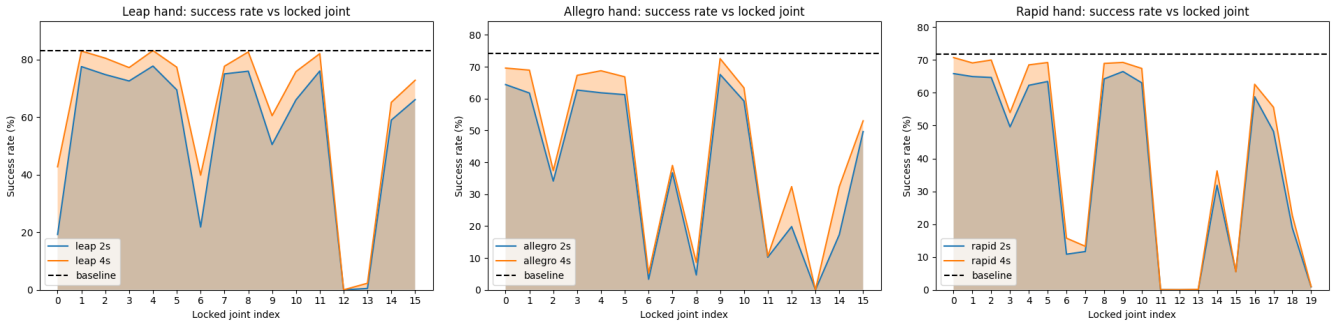

Fig. 7. Zero-shot performance under joint locking. For LEAP and Allegro, joint indices 0–15 are sequentially locked, and for RAPID 0–19. We report success rates for 2-s and 4-s execution windows and compare against the zero-shot canonical baseline.

policies are trained with 4096 parallel environments episodes and evaluated on both *zero-shot generalization* on the canonical hand and a 32-variant test set across LEAP, Allegro, and RAPID hands. For each evaluation, we execute the policy across 32 parallel environments for a total of 100 episodes.

As shown in TABLE II, DexFormer consistently outperforms LSTM- and GRU-based baselines in grasping success rate after 40k training episodes, addressing Q1. Moreover, it demonstrates strong zero-shot generalization across heterogeneous robotic hands, addressing Q2.

TABLE II
COMPARISON WITH LSTM AND GRU-BASED BASELINES.

Hand	Setting	LSTM	GRU	Ours
LEAP	canonical	66.81	58.91	**83.25**
	32 variants	66.72	57.38	**86.84**
Allegro	canonical	65.38	25.81	**74.19**
	32 variants	62.44	24.97	**71.94**
RAPID	canonical	46.72	45.06	**71.69**
	32 variants	44.22	53.59	**77.09**
Average	Combined	58.72	44.29	**77.50**

To answer Q3, we assess the effect of temporal context by comparing DexFormer policies with a single history step and with a 5-step history. As shown in Table III, under an equal 40k-episode training budget, incorporating observation–action histories improves zero-shot performance for both the LEAP and Allegro hands.

TABLE III
COMPARISON OF HISTORY LENGTH.

Hand	Setting	1-step	5-step (Ours)
LEAP	canonical	82.72	**83.25**
	32 variants	83.34	**86.84**
Allegro	canonical	56.47	**74.19**
	32 variants	55.16	**71.94**
RAPID	canonical	**77.59**	71.69
	32 variants	**82.75**	77.09
Average	Combined	73.00	**77.50**

We study the effect of morphological diversity during training by varying the number of distinct training embodiments used. For this experiment, we trained three policies and used single GPU per each hand type. As summarized in Table IV, for a 25k-episode training, increasing embodiment diversity substantially improves zero-shot grasping performance on unseen hands, indicating that exposure to heterogeneous embodiments during training enhances cross-embodiment generalization, addressing Q4.

TABLE IV
ABLATION ON TRAINING SET EMBODIMENT DIVERSITY.

Hand	Setting	25 Hands	50 Hands	100 Hands (Ours)
LEAP	canonical	81.59	80.28	**90.12**
	32 variants	81.44	84.59	**91.31**
Allegro	canonical	80.34	77.84	**80.81**
	32 variants	77.12	74.44	**78.38**
RAPID	canonical	82.09	80.00	**84.56**
	32 variants	78.47	78.88	**79.41**
Average	Combined	80.18	79.34	**84.09**

To answer Q5, we further analyze the scalability of DexFormer with respect to environment-level parallelism. As shown in Table V, under a 30k-episode training budget and using 3 GPUs for distributed training, increasing the number of parallel environments per GPU improves performance for LEAP and Allegro hands. However, we noticed some performance drop for zero-shot transfer to the canonical RAPID hand and its variants, which we attribute to an imbalance in morphology statistics during training.

Locking individual joints induces structured degradation patterns that reflect the anatomical role and kinematic importance of each DoF, shown in Fig. 7. We evaluate using the optimal DexFormer checkpoint reported in Table II. Across all embodiments, distal flexion joints (PIP/DIP) and low-leverage MCP abduction joints cause mild reductions, while basal flexion and thumb CMC joints produce pronounced drops, consistent with their contribution to establishing stable contact and opposition. Notably, all impaired variants achieve success rates that are lower than, or at most match, the canonical hand's zero-shot performance, indicating no compensatory gain from joint removal. The consistent gap between 2-s and

TABLE V
ABLATION ON NUMBER OF ENVIRONMENTS IN PARALLEL.

Hand	Setting	1024/GPU	2048/GPU	4096/GPU (Ours)
LEAP	canonical	66.22	82.53	**87.00**
	32 variants	69.03	80.66	**88.78**
Allegro	canonical	67.16	70.78	**77.50**
	32 variants	63.94	69.12	**77.12**
RAPID	canonical	**74.34**	69.91	69.72
	32 variants	**79.56**	76.97	77.72
Average	canonical	69.24	74.41	**78.07**
	32 variants	70.84	75.58	**81.21**

4-s execution windows suggests that extended rollout enables partial compensation even under impaired morphology, addressing Q6.

D. Real-world evaluation

We use a LEAP hand mounted on Franka arm for real-world experiments. To maintain consistency with the simulated ray-casting observations, the real-world system employs two identically mounted Intel RealSense D435 cameras. The resulting depth measurements are fused through ICP and clipped to the hand workspace to produce a coherent point-cloud representation of both the dexterous hand and manipulated objects. The Franka arm runs its joint-space controller at 1000 Hz, and the learned policy is evaluated at 10 Hz. The real-world setup is shown as in Fig. 8.

Fig. 8. Real-world evaluation of the DexFormer policy.

For smooth sim-to-real transfer, we perform offline distillation rather than online distillation, enabling efficient data acquisition and stable training. We recorded 2000 episodes of expert demonstrations with a 158-dimensional observation space. The student MLP network is optimized with Adam using a learning rate of 0.001. The deployed policy can successfully lift the object cube into target position.

V. CONCLUSION

We present DexFormer, a history-conditioned transformer policy for cross-embodiment dexterous manipulation. By conditioning on observation–action histories, DexFormer implicitly infers morphology and dynamics, enabling a single policy to generalize across heterogeneous robotic hands without requiring embodiment identifiers or dedicated decoder heads. Extensive experiments demonstrate that DexFormer (i) outperforms GRU- and LSTM-based baselines, (ii) achieves strong zero-shot transfer across LEAP, Allegro, and RAPID hands and their variants, and (iii) benefits from temporal context, morphology diversity, and environment-level parallelism. These findings provide evidence that dynamics-aware temporal inference is an effective mechanism for cross-embodiment generalization. Real-world evaluations further support the practicality of the approach, indicating that morphology-agnostic dexterous manipulation can extend beyond simulation. Overall, DexFormer offers a scalable path toward unified manipulation policies applicable across diverse embodiments and deployment scenarios.

VI. LIMITATIONS

While DexFormer demonstrates strong cross-embodiment generalization for embodiment variations, several limitations remain. First, our current training regime focuses on a limited set of object geometries and mass properties, leading to insufficient object-level generalization. Extending training to larger, more diverse object collections and incorporating multi-expert distillation or mixture-of-experts could improve robustness and transferability to real-world manipulation scenarios. Second, we observe a modest performance drop on higher-DoF embodiments such as RAPID Hand under zero-shot settings. This suggests that more sophisticated architectural or scaling strategies may be beneficial, including deeper temporal modeling, improved action embeddings, and higher degrees of environment-level parallelism. Furthermore, due to current limitations in Isaac Lab, embodiments with distinct kinematic topologies are trained on separate GPUs. Enabling mixed buffer or centralized gradient accumulation across embodiments may reduce gradient variance and improve generalization.

We consider addressing these limitations an important direction for future work, particularly toward foundation-style models for dexterous manipulation. More broadly, we aim to promote a cross-embodiment learning paradigm in which scalable RL training enables high-DoF, morphologically diverse embodiments to be trained at scale, while downstream users can either post-train, finetune, or incorporate residual policies to further adapt to new embodiments and tasks. We view such a path as a step toward more generalized cross-embodiment manipulation policies.

REFERENCES

[1] Ilge Akkaya, Marcin Andrychowicz, Maciek Chociej, Mateusz Litwin, Bob McGrew, Arthur Petron, Alex Paino, Matthias Plappert, Glenn Powell, Raphael Ribas, et al. Solving rubik's cube with a robot hand. *arXiv preprint arXiv:1910.07113*, 2019.

[2] OpenAI: Marcin Andrychowicz, Bowen Baker, Maciek Chociej, Rafal Jozefowicz, Bob McGrew, Jakub Pachocki, Arthur Petron, Matthias Plappert, Glenn Powell, Alex Ray, et al. Learning dexterous in-hand manipulation. *The International Journal of Robotics Research*, 39 (1):3–20, 2020.

[3] Sirui Chen, Albert Wu, and C. Karen Liu. Synthesize dexterous nonprehensile pregrasp for ungraspable objects. 2023. doi: 10.1145/3588432.3591528.

[4] Tao Chen, Megha Tippur, Siyang Wu, Vikash Kumar, Edward Adelson, and Pulkit Agrawal. Visual dexterity: In-hand reorientation of novel and complex object shapes. 2022. doi: 10.1126/scirobotics.adc9244.

[5] Zeyuan Chen, Qiyang Yan, Yuanpei Chen, Tianhao Wu, Jiyao Zhang, Zihan Ding, Jinzhou Li, Yaodong Yang, and Hao Dong. Clutterdexgrasp: A sim-to-real system for general dexterous grasping in cluttered scenes, 2025.

[6] Nolan Fey, Gabriel B Margolis, Martin Peticco, and Pulkit Agrawal. Bridging the sim-to-real gap for athletic loco-manipulation. *arXiv preprint arXiv:2502.10894*, 2025.

[7] Ashish Kumar, Zipeng Fu, Deepak Pathak, and Jitendra Malik. Rma: Rapid motor adaptation for legged robots. *arXiv preprint arXiv:2107.04034*, 2021.

[8] Ashish Kumar, Zhongyu Li, Jun Zeng, Deepak Pathak, Koushil Sreenath, and Jitendra Malik. Adapting rapid motor adaptation for bipedal robots. In *2022 IEEE/RSJ International Conference on Intelligent Robots and Systems (IROS)*, pages 1161–1168, 2022. doi: 10.1109/IROS47612.2022.9981091.

[9] Taeyoon Lee, Jaewoon Kwon, Patrick M Wensing, and Frank C Park. Robot model identification and learning: A modern perspective. *Annual Review of Control, Robotics, and Autonomous Systems*, 7, 2023.

[10] Yichao Liang, Kevin Ellis, and João Henriques. Rapid motor adaptation for robotic manipulator arms. In *Proceedings of the IEEE/CVF Conference on Computer Vision and Pattern Recognition (CVPR)*, pages 16404–16413, June 2024.

[11] Min Liu, Deepak Pathak, and Ananye Agarwal. Locoformer: Generalist locomotion via long-context adaptation. *arXiv preprint arXiv:2509.23745*, 2025.

[12] Xueyi Liu, He Wang, and Li Yi. Dexndm: Closing the reality gap for dexterous in-hand rotation via joint-wise neural dynamics model, 2025.

[13] Tyler Ga Wei Lum, Martin Matak, Viktor Makoviychuk, Ankur Handa, Arthur Allshire, Tucker Hermans, Nathan D. Ratliff, and Karl Van Wyk. Dextrah-g: Pixels-to-action dexterous arm-hand grasping with geometric fabrics, 2024.

[14] NVIDIA Research. Isaac lab: A gpu-accelerated simulation framework for multi-modal robot learning, 2025.

[15] Austin Patel and Shuran Song. Get-zero: Graph embodiment transformer for zero-shot embodiment generalization. In *2025 IEEE International Conference on Robotics and Automation (ICRA)*, pages 14262–14269. IEEE, 2025.

[16] Haozhi Qi, Ashish Kumar, Roberto Calandra, Yi Ma, and Jitendra Malik. In-hand object rotation via rapid motor adaptation. In *Conference on Robot Learning*, pages 1722–1732. PMLR, 2023.

[17] Kenneth Shaw, Ananye Agarwal, and Deepak Pathak. Leap hand: Low-cost, efficient, and anthropomorphic hand for robot learning. *Robotics: Science and Systems (RSS)*, 2023.

[18] Ritvik Singh, Arthur Allshire, Ankur Handa, Nathan Ratliff, and Karl Van Wyk. Dextrah-rgb: Visuomotor policies to grasp anything with dexterous hands, 2024.

[19] Nikhil Sobanbabu, Guanqi He, Tairan He, Yuxiang Yang, and Guanya Shi. Sampling-based system identification with active exploration for legged robot sim2real learning. *arXiv preprint arXiv:2505.14266*, 2025.

[20] Zhaoliang Wan, Zetong Bi, Zida Zhou, Hao Ren, Yiming Zeng, Yihan Li, Lu Qi, Xu Yang, Ming-Hsuan Yang, and Hui Cheng. Rapid hand: A robust, affordable, perception-integrated, dexterous manipulation platform for generalist robot autonomy. *arXiv preprint arXiv:2506.07490*, 2025.

[21] Jun Wang, Ying Yuan, Haichuan Che, Haozhi Qi, Yi Ma, Jitendra Malik, and Xiaolong Wang. Lessons from learning to spin "pens", 2024.

[22] Yuhan Wang, Yu Li, Yaodong Yang, and Yuanpei Chen. Dexterous non-prehensile manipulation for ungraspable object via extrinsic dexterity, 2025.

[23] Zhenyu Wei, Zhixuan Xu, Jingxiang Guo, Yiwen Hou, Chongkai Gao, Zhehao Cai, Jiayu Luo, and Lin Shao. D (r, o) grasp: A unified representation of robot and object interaction for cross-embodiment dexterous grasping. *arXiv preprint arXiv:2410.01702*, 2024.

[24] Zhiyuan Wu, Rolandos Alexandros Potamias, Xuyang Zhang, Zhongqun Zhang, Jiankang Deng, and Shan Luo. Cedex: Cross-embodiment dexterous grasp generation at scale from human-like contact representations. *arXiv preprint arXiv:2509.24661*, 2025.

[25] Lixin Xu, Zixuan Liu, Zhewei Gui, Jingxiang Guo, Zeyu Jiang, Tongzhou Zhang, Zhixuan Xu, Chongkai Gao, and Lin Shao. Dexsingrasp: Learning a unified policy for dexterous object singulation and grasping in densely cluttered environments, 2025.

[26] Haoqi Yuan, Bohan Zhou, Yuhui Fu, and Zongqing Lu. Cross-embodiment dexterous grasping with reinforcement learning. *arXiv preprint arXiv:2410.02479*, 2024.

[27] Ying Yuan, Haichuan Che, Yuzhe Qin, Binghao Huang, Zhao-Heng Yin, Kang-Won Lee, Yi Wu, Soo-Chul Lim, and Xiaolong Wang. Robot synesthesia: In-hand manipulation with visuotactile sensing, 2023.

[28] Heng Zhang, Kevin Yuchen Ma, Mike Zheng Shou, Weisi Lin, and Yan Wu. Cross-embodiment dexterous hand articulation generation via morphology-aware learning. *arXiv preprint arXiv:2510.06068*, 2025.

[29] Hui Zhang, Sammy Christen, Zicong Fan, Otmar Hilliges, and Jie Song. Graspxl: Generating grasping motions for diverse objects at scale, 2024.

[30] Zhe Zhao, Haoyu Dong, Zhengmao He, Yang Li, Xinyu Yi, and Zhibin Li. Closing the reality gap: Zero-shot sim-to-real deployment for dexterous force-based grasping and manipulation, 2026.

[31] Shaoting Zhu, Ziwen Zhuang, Mengjie Zhao, Kun-Ying Lee, and Hang Zhao. Hiking in the wild: A scalable perceptive parkour framework for humanoids. *arXiv preprint arXiv:2601.07718*, 2026.

APPENDIX

A. Cross-embodiment Training

We employ Automatic Domain Randomization (ADR) to progressively increasing noise levels on joint positions, joint velocities, fingertip states, point-cloud observations, and gravity as the policy performance improves. The ADR curve during training is shown as in Fig. 9. The learning curves for average reward and success with respect to training episodes are reported in Fig. 10 and 11. As can be seen, our DexFormer policy outperforms LSTM-based and GRU-based policy by training efficiency (curves rise faster) and accuracy.

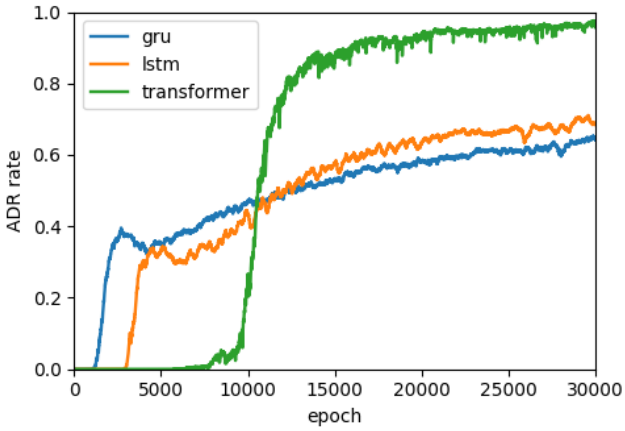

Fig. 9. ADR rate with respect to training episodes

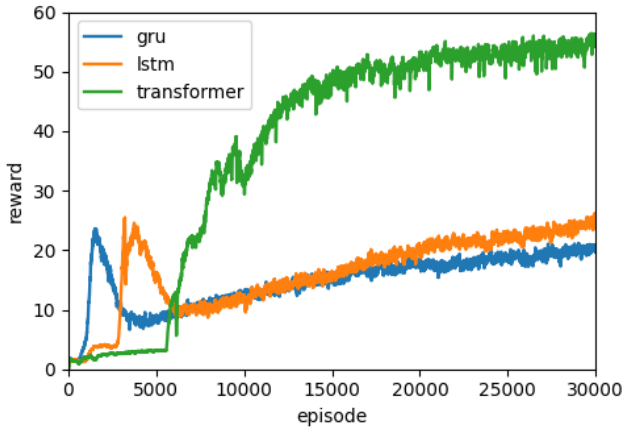

Fig. 10. Reward with respect to training episodes

B. Real-world evaluation

For real world experiments, we use several objects during evaluation: an orange cube, a red mug, a yellow cube, a hamster toy, a cat toy, a dodecahedron, a icosahedron, and a package box, as shown in Fig. 12.

We first test our distilled DexFormer Policy on canonical LEAP hand. The qualitative grasping results are shwon as

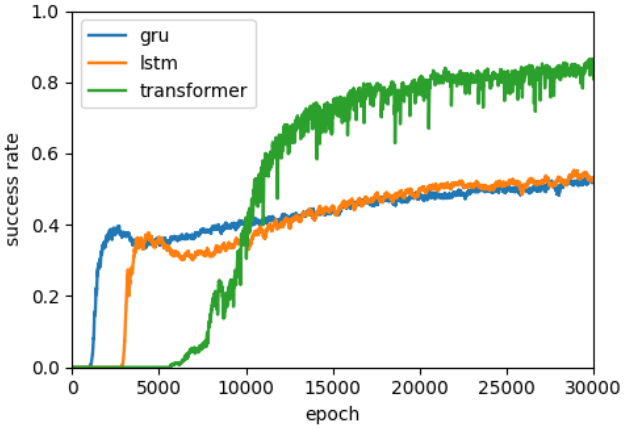

Fig. 11. Success rate with respect to training episodes

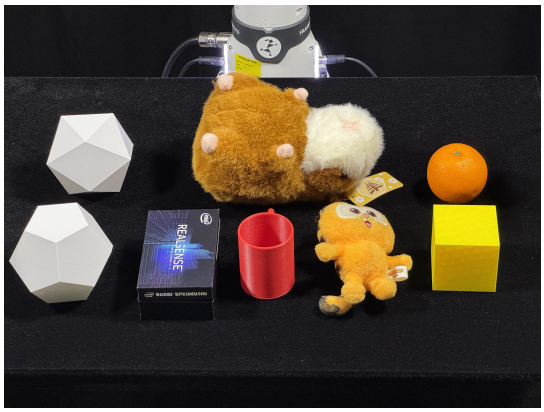

Fig. 12. Objects used for real-world experiments

Fig. 13. The real-world quantitative results are listed in TABLE VI, showing the success rate and execution average time.

TABLE VI
GRASPING SUCCESS RATE ACROSS OBJECTS.

Object	Success Rate	Avg. Time (sec)
Orange fruit	4/5	7.45
Red mug	2/5	6.32
Yellow cube	3/5	7.34
Dodecahedron	1/5	6.10
Icosahedron	2/5	6.45
Large hamster	2/5	4.93
Cat toy	3/5	6.23
Package box	3/5	7.90

We then test a distilled version of DexFormer policy rolled out on three real-world LEAP hand variants. We construct physical LEAP hand variants by removing selected finger joint structures from the canonical configuration, shown in Fig. 14. From left to right, the variants remove 1 DoF on the ring finger, 2 DoFs on the ring and middle fingers, and 3 DoFs on the index, middle, and ring fingers, respectively. The qualitative grasping results are shown in Fig. 15.

(a) Grasping an orange fruit.

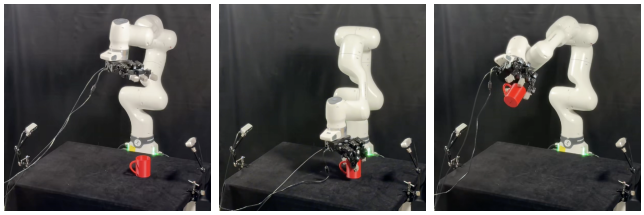

(b) Grasping a red mug

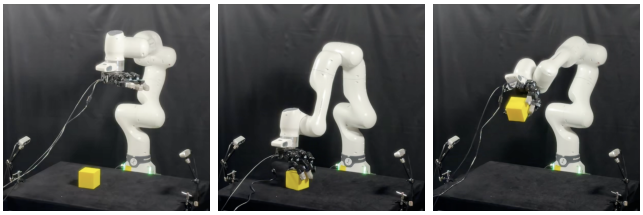

(c) Grasping a yellow cube

(d) Grasping a large hamster toy

(e) Grasping a regular dodecahedron (12-faced polyhedron)

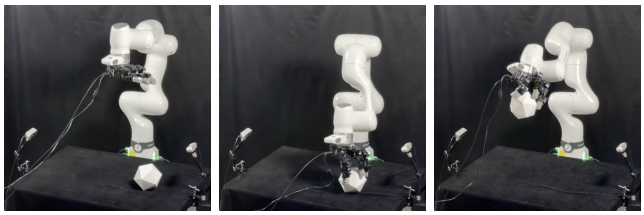

(f) Grasping regular icosahedron (20-faced polyhedron)

(g) Grasping a smaller cat toy

(h) Grasping a package box in the middle

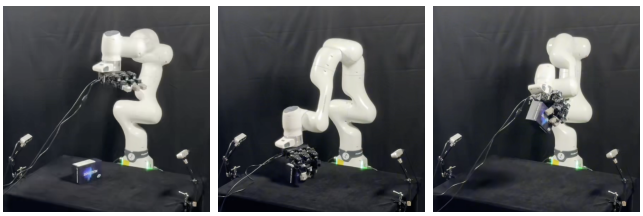

(i) Grasping a package box to the left

(j) Grasping a package box to the right

Fig. 13. Qualitative grasping results on canonical LEAP hand grasping different objects.

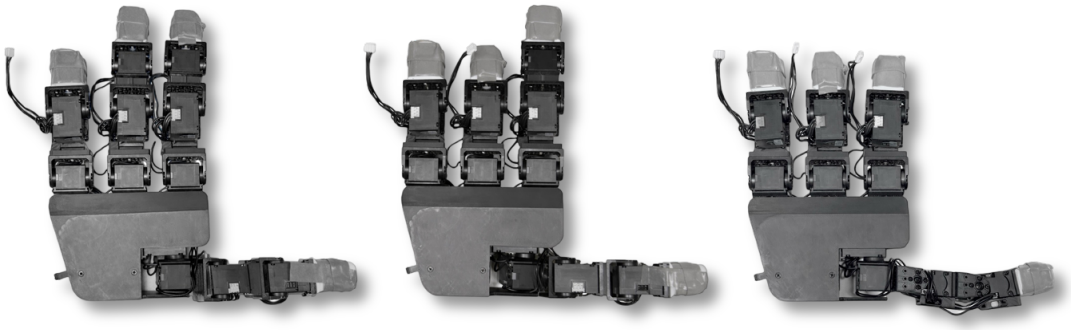

Fig. 14. Real-world LEAP hand variants with reduced degrees of freedom.

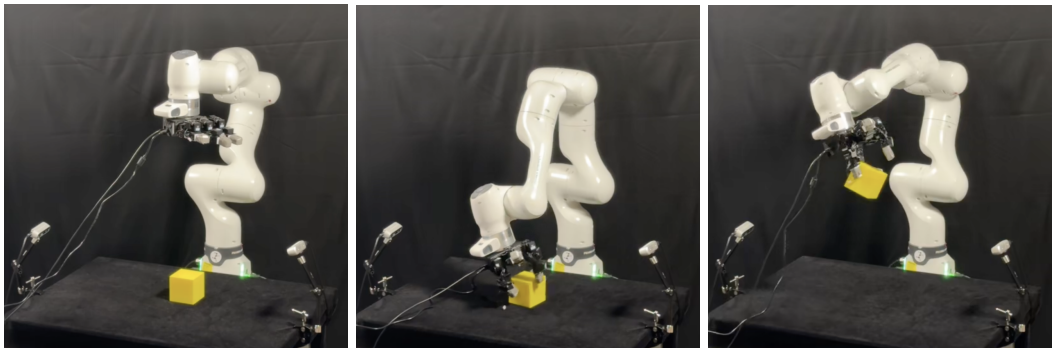

(a) LEAP variant with 1 DoF removed.

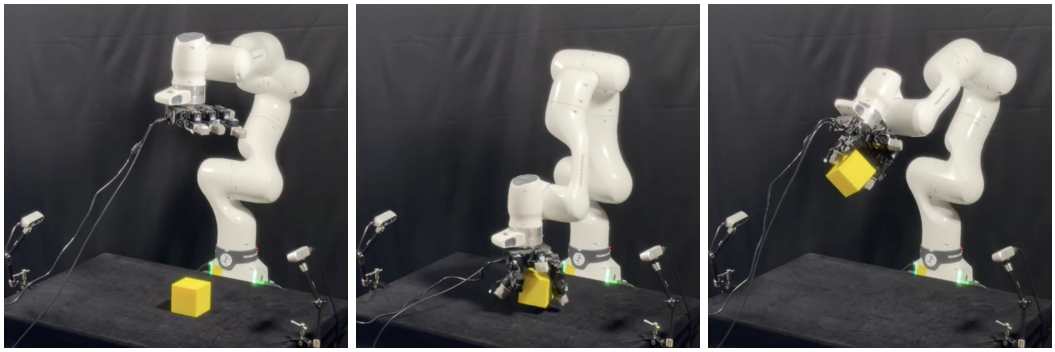

(b) LEAP variant with 2 DoFs removed.

(c) LEAP variant with 3 DoFs removed.

Fig. 15. Evaluation on LEAP hand variants with reduced degrees of freedom.